INTERNATIONAL JOURNAL FOR NUMERICAL METHODS IN FLUIDS
Int. J. Numer. Meth. Fluids 2002; **40**:1303–1325 (DOI: 10.1002/fld.419)

An approximate projection method for incompressible flow

David E. Stevens*,† Stevens T. Chan and Phil Gresho

L-98, Lawrence Livermore National Laboratory, P.O. Box 808, CA 94551 Livermore, U.S.A.

SUMMARY

This paper presents an approximate projection method for incompressible flows. This method is derived from Galerkin orthogonality conditions using equal-order piecewise linear elements for both velocity and pressure, hereafter Q1Q1. By combining an approximate projection for the velocities with a variational discretization of the continuum pressure Poisson equation, one eliminates the need to filter either the velocity or pressure fields as is often needed with equal-order element formulations. This variational approach extends to multiple types of elements; examples and results for triangular and quadrilateral elements are provided. This method is related to the method of Almgren *et al.* (*SIAM J. Sci. Comput.* 2000; 22:1139–1159) and the PISO method of Issa (*J. Comput. Phys.* 1985; 62:40–65). These methods use a combination of two elliptic solves, one to reduce the divergence of the velocities and another to approximate the pressure Poisson equation. Both Q1Q1 and the method of Almgren *et al.* solve the second Poisson equation with a weak error tolerance to achieve more computational efficiency.

A Fourier analysis of Q1Q1 shows that a consistent mass matrix has a positive effect on both accuracy and mass conservation. A numerical comparison with the widely used Q1Q0 (piecewise linear velocities, piecewise constant pressures) on a periodic test case with an analytic solution verifies this analysis. Q1Q1 is shown to have comparable accuracy as Q1Q0 and good agreement with experiment for flow over an isolated cubic obstacle and dispersion of a point source in its wake. Copyright © 2002 John Wiley & Sons, Ltd.

1. INTRODUCTION

Projection methods are popular techniques for simulating incompressible or quasi-incompressible flow. This is due to their simple description of the flow in terms of primitive variables (such as velocities, pressures and temperatures), their algorithmic simplicity in that no variable transformations are required and no sub-cycling of the pressure (such as with artificial compressible methods) is needed in time. Although they require the solution of an elliptic Poisson equation, they are computationally efficient due to recent advances in linear algebra, such as the incorporation of advanced multigrid methods. References on recent developments in projection methods can be found in Almgren *et al.* [1] and Gresho and Chan [2].

* Correspondence to: D. E. Stevens, L-98, Lawrence Livermore National Laboratory, P.O. Box 808, CA 94551 Livermore, U.S.A.
† E-mail: stevens9@llnl.gov

Contract/grant sponsor: U.S. Department of Energy; contract/grant number: W-7405-Eng-48

Received August 2001
Revised 24 June 2002

The equations modelled in this study involve evolution equations for momentum and an advected scalar subject to an incompressibility constraint.

$$\frac{\partial u_i}{\partial t} + u_j \frac{\partial u_i}{\partial x_j} + \frac{\partial \overline{u_i' u_j'}}{\partial x_j} + \frac{\partial p}{\partial x_i} = K \frac{\partial^2 u_i}{\partial x_j^2} \tag{1}$$

$$\frac{\partial u_i}{\partial x_i} = 0 \tag{2}$$

$$\frac{\partial c}{\partial t} + u_j \frac{\partial c}{\partial x_j} + \frac{\partial \overline{u_j' c'}}{\partial x_j} = K_c \frac{\partial^2 c}{\partial x_j^2} \tag{3}$$

In the above equations, turbulent stress $\overline{u_i' u_j'}$ and scalar flux $\overline{u_j' c'}$ are parameterized (when turbulent effects are present) via an appropriate turbulence model and a constant viscosity K for velocity and K_c for the scalar are used. The continuum pressure Poisson equation (PPE) is derived by combining Equations (1) and (2) to obtain an equation for a pressure potential, p:

$$-\frac{\partial}{\partial x_i}\left(u_j \frac{\partial u_i}{\partial x_j} + \frac{\partial \overline{u_i' u_j'}}{\partial x_j} - K \frac{\partial^2 u_i}{\partial x_j^2} \right) = \frac{\partial^2 p}{\partial x_i^2} \tag{4}$$

The term projection method arises from the fact that a velocity field can be decomposed into a divergence free field and a gradient of a scalar. Methods which solve for such a scalar, often by inverting a Poisson problem and subtracting the solution's gradient off of the original velocity field, are called projection methods. Many of the various projection methods are differentiated via the manner in which they discretize and combine the temporal discretization of Equation (1) with the spatial discretization of Equations (2) and (4). An analysis of five such methods is presented in Almgren *et al.* [1], hereafter referred to as ABC. Our method is an extension of their fifth method, **P5**. Both methods discretize the above equations in such a way that both Equations (2) and (4) are numerically approximated.

This paper first describes and motivates the ideas behind this method. Its ideas are shown to be applicable to triangles and quadrilaterals in 2D and tetrahedrons and hexahedrons in 3D. This is followed by a results section where tests are performed on both a simple periodic test case where an analytic solution is known and a challenging test case: the dispersion of a tracer released behind a cube embedded in a turbulent flow field. The test cases are also used to compare this method with a more traditional and widely used staggered grid approach. We conclude with a summary and interpretation of the results.

2. THEORY

2.1. The approximate projection

Our numerical method employs the linearized implicit approach of Gresho and Chan [2], where the momentum and scalar equations are discretized as

$$M\left(\frac{u^{n+1} - u^n}{\Delta t}\right) + (K + N(u^n))(\theta u^{n+1} + (1-\theta)u^n) = -Gp^{n-1/2} \tag{5}$$

$$M\left(\frac{c^{n+1} - c^n}{\Delta t}\right) + (K + N(u^n))(\theta c^{n+1} + (1-\theta)c^n) = 0 \tag{6}$$

In this formulation, for simplicity only Dirichlet boundary conditions are being considered. Additional boundary conditions can be handled by adding additional terms to the RHS of both equations and do not complicate the following analysis. Here M, K, N and G are the mass, diffusion, advection and pressure gradient matrices and θ is a time-stepping parameter ($0 \leqslant \theta \leqslant 1$). Each of these matrices is sparse and is obtained from Galerkin's method of weighted residuals using piecewise linear basis functions (hereafter denoted as ϕ_i) defined on either triangles or quadrilaterals in 2D and tetrahedrons or hexahedrons in 3D with the property $\phi_i(x_j) = \delta_{ij}$. In a later step, the first-order error of using $p^{n-1/2}$ is corrected by a projection. The mass matrix can also be 'lumped' by adding all off-diagonal terms onto the diagonal. This mass matrix is denoted by M_L and results in a completely explicit set of equations if $\theta = 0$.

We seek to improve on Gresho and Chan's approach (hereafter referred to as Q1Q0 with respect to the order of elements used for velocity and pressure) which uses a piecewise constant basis function defined on elements for the pressure (ψ) and integrates by parts to yield the pressure gradient matrix.

$$G_{ij}^k = -\int \frac{\partial \phi_i}{\partial x_k} \psi_j \, \mathrm{d}A \tag{7}$$

where ϕ_i is the trial function. Conservation of mass is expressed via

$$D_{ji}^k u_j^k = 0 \tag{8}$$

For Q1Q0, this divergence matrix is the transpose of the pressure gradient matrix, $G^{\mathrm{T}} = D$. Q1Q0 with lumped mass, $M = M_L$, uses an exact projection where mass conservation is always discretely preserved, i.e. $Du^{n+1} = 0$. The Q1Q0 exact projection is found by combining Equations (5) and (8) to get a diagnostic equation for the pressure that requires inverting a discrete pressure Poisson matrix $G^{\mathrm{T}} M_L^{-1} G$ every timestep. This matrix is sparse and easy to construct. Unfortunately, it is ill-conditioned in that there exist 'checkerboard' modes in the velocities and/or the pressure field [3, 4]. Good performance can be achieved by 'stabilizing' this matrix with smoothers or other filters (see References [5, 6] for a review of this topic). Unfortunately, this often comes at the price of accuracy in the solution and at least a partial loss of the discrete mass conservation property.

In our equal-order approach (hereafter referred to as Q1Q1), we discretize the pressure gradient term directly to get

$$G_{ij}^k = \int \phi_i \frac{\partial \phi_j}{\partial x_k} \, \mathrm{d}A \tag{9}$$

and have an analogous expression for conservation of mass

$$D_{ij}^k = \int \phi_i \frac{\partial \phi_j}{\partial x_k} \, \mathrm{d}A \tag{10}$$

However, mass conservation via our Q1Q1 approach is a weak one and is only approximately enforced, and hence the name of approximate projection method. The Q1Q0 exact projection satisfies a discrete version of both Equations (5) and (8). However for Q1Q1, this is not true and if one desires to solve only one elliptic equation, one must choose either to project u for mass conservation or project the acceleration of u to approximate the PPE. This results in numerical difficulties, since errors are observed in the pressure field if the pressure Poisson

equation is solely defined to minimize the divergence of the velocities. Similarly, the velocities suffer, if one derives the pressure Poisson equation solely from the PPE. Our Q1Q1 approach solves this problem through the use of two Poisson solves which interpret both the PPE and conservation of mass in a variational manner. Since the Poisson operator is derived by a well-conditioned operator, Q1Q1 eliminates the need for numerical filters to improve the performance of numerical linear system solvers.

Another improvement of Q1Q1 is the use of midpoint in time values for the advection term, $N(u^{n+1/2})$. This removes a first-order temporal error in the discretization and will later be seen to improve the results. Unfortunately, this improvement results in a cost increase, due to the fact that one must first compute a timestep as a predictor to obtain $u^{n+1/2}$. This improvement is worthwhile in cases where the data are sufficiently smooth and there are no other first-order errors.

Our method seeks to avoid the above-mentioned problems with either the velocity or pressure by using two projection steps. First we invert a version of Equation (5) which uses the previous value of the pressure at $t^{n-1/2}$

$$M\left(\frac{u^* - u^n}{\Delta t}\right) + (K + N(u^n))(\theta u^* + (1-\theta)u^n) = -Gp^{n-1/2} \tag{11}$$

If we are computing the very first timestep, the value of $p^{-1/2}$ can be found by inverting:

$$D((K + N(u^0))u^0) = Lp^{-1/2} \tag{12}$$

Then in the first projection step, we numerically project u^* which involves solving for an intermediate pressure $\phi = \tilde{p} - p^{n-1/2}$ via

$$L\phi = Du^*/\Delta t \tag{13}$$

where $L_{ij} = \int(\partial\phi_i/\partial x_k)(\partial\phi_j/\partial x_k)\,\mathrm{d}A$ is the standard finite element Laplacian and then applying its pressure gradient to the velocities via

$$M\left(\frac{u^{n+1} - u^*}{\Delta t}\right) = -G\phi \tag{14}$$

For the case, where $N(u^{n+1/2})$ is desired, one repeats Equations (11)–(14) using $N(u^{n+1/2})$ where $u^{n+1/2} = (u^n + u^{n+1})/2$ instead of $N(u^n)$ in Equation (11). After obtaining u^{n+1}, we compute a final pressure, $p^{n+1/2}$, which seeks to force the discrete pressure to adhere to Equation (4),

$$Lp^{n+1/2} = DM^{-1}H^{n+1/2} \tag{15}$$

where $H^{n+1/2} = -(K + N(u^{n+1/2}))(\theta u^* + (1-\theta)u^n)$. Here we use an important observation from ABC: Since $\tilde{p} = \phi + p^{n-1/2}$ is in practice very close to the desired $p^{n+1/2}$, one can solve this equation iteratively using $\tilde{p}$ as a first guess and with a much more relaxed tolerance than the previous elliptic solve. Typically, we use a relative residual of $1.e-8$ for the first projection and $1.e-2$ for the second. Since L is much better conditioned than $G^{\mathrm{T}}M_L^{-1}G$, the overall linear algebra cost is lower and often one can use methods such as multigrid (see for instance, Reference [7]) that are often ineffective for the case of non-stabilized

$G^{\mathrm{T}}M_L^{-1}G$. An important practical extension of this approach is that it is not limited to a particular type of element. The following analysis of the effectiveness of the projection is done for both triangular piecewise-linear (referred to as P1P1) and the quadrilateral bilinear Q1Q1 elements.

An analysis of the performance of the approximate projection in damping divergent modes follows. First, the exact projection ($G^{\mathrm{T}}u^{n+1}=0$) for Q1Q0 can be summarized via the following recurrence relation:

$$\begin{aligned} u^{n+1} &= u^n + \Delta t M_L^{-1}(H^{n+1/2} - Gp^{n+1/2}) \\ Gp^{n+1/2} &= G(G^{\mathrm{T}}M_L^{-1}G)^{-1}G^{\mathrm{T}}M_L^{-1}H^{n+1/2} \end{aligned} \tag{16}$$

If we define the projection operator, $P^L = I - M_L^{-1}G(G^{\mathrm{T}}M_L^{-1}G)^{-1}G^{\mathrm{T}}$, this can be summed to express u^n in terms of u^0 and the forcings $H^{i-1/2}$:

$$\begin{aligned} u^{n+1} &= u^0 + \Delta t \sum_{i=0}^{n} P^L M_L^{-1} H^{i+1/2} \\ Gp^{n+1/2} &= M_L(I - P^L)M_L^{-1}H^{n+1/2} \end{aligned} \tag{17}$$

The fact that the forcing $H^{n+1/2}$ was projected rather than u^{n+1} is immaterial for the Q1Q0 exact projection. We can generalize this to arbitrary, D, G, and M matrices by using the more general exact projection operator $P = I - M^{-1}G(DM^{-1}G)^{-1}D$. This operator has the property that if $u = P\tilde{u}$, then $Du = 0$; P projects $\tilde{u}$ to a divergence free sub-space.

An approximate projection that is directly motivated by this form of Q1Q0, would be to define the pressure gradient via

$$Gp^{n+1/2} = GL^{-1}DM^{-1}H^{n+1/2} \tag{18}$$

which results in the method

$$u^{n+1} = u^0 + \Delta t \sum_{i=0}^{n} \tilde{P}M^{-1}H^{i+1/2} \tag{19}$$

$$Gp^{n+1/2} = M(I - \tilde{P})M^{-1}H^{n+1/2} \tag{20}$$

$$\tilde{P} = I - M^{-1}GL^{-1}D \tag{21}$$

Note the presence of the mass matrix M in $\tilde{P}$. It will be shown to have an important effect on the performance of the projection. Unfortunately for $\tilde{P}$, there are non-zero divergent components of $M^{-1}H^{i-1/2}$ which are not completely eliminated by the projection that may accumulate resulting in a degraded velocity field. This is the fourth method presented in ABC and was shown to have pathological behaviour.

Our approximate projection method, like the fifth method in ABC, avoids this accumulation by combining its first projection step which can be expressed as

$$u^{n+1} = u^* - M^{-1}GL^{-1}Du^* = \tilde{P}u^* \tag{22}$$

with a second projection step of the forcing term $H^{n+1/2}$ to yield the recurrence relations:

$$u^{n+1} = \tilde{P}(u^n + \Delta t M^{-1} H^{n+1/2} - \Delta t M^{-1} G p^{n-1/2}) \tag{23}$$

$$G p^{n+1/2} = M(I - \tilde{P}) M^{-1} H^{n+1/2} \tag{24}$$

The expression for $Gp^{n+1/2}$ is the same as Equation (20) for the pathological projection whereas the projection operator is continually applied to u to force it towards a divergence free state. This is shown by the summed recurrence relationship for u^n

$$\begin{aligned} u^n = \tilde{P}^n(u^0 - \Delta t M^{-1} G p^{-1/2}) + \Delta t \tilde{P} M^{-1} H^{n+1/2} \\ + \Delta t \sum_{i=1}^{n} \tilde{P}^i (2\tilde{P} - I) M^{-1} H^{n-i+1/2} \end{aligned} \tag{25}$$

This indicates that the final velocity field is the sum of an initial condition and forcing terms that have been processed numerous times via the $\tilde{P}$ operator. As long as this operator damps divergent modes, mass conservation will be maintained. The Fourier analysis in the next subsection verifies this damping property.

2.2. *Fourier analysis of the approximate projection*

One estimate of the performance of this approximate projection method can be determined by examining the effect of computing the projection of the gradient operator applied to a Fourier component of an arbitrary scalar ψ. Since for periodic problems, the Fourier components are eigenvectors of G, D, M and L, one can easily determine the damping applied to each Fourier component. The behaviour for both the exact projection, $P = I - M^{-1}G(DM^{-1}G)^{-1}D$, and the approximate projection, $\tilde{P} = I - M^{-1}GL^{-1}D$ can be found simply by substituting in the appropriate relationship for each matrix. For the mass and Laplacian matrices, this relationship is given by

$$\begin{aligned} Mz &= \lambda_M z \\ Lz &= \lambda_L z \end{aligned} \tag{26}$$

where λ_L and λ_M are the eigenvalues of the Laplacian and Mass operators and z is the Fourier component. For the gradient operator, one uses the relationship:

$$Gz = \begin{bmatrix} \lambda_x \\ \lambda_y \end{bmatrix} z \tag{27}$$

where λ_x and λ_y are respectively the Fourier eigenvalues of the x and y discrete derivatives. These same derivative eigenvalues are also used for the divergence operator. The result of this Fourier analysis is that the projection operators can be expressed in matrix

notation as

$$P = \frac{1}{\lambda_x^2 + \lambda_y^2} \begin{bmatrix} \lambda_y^2 & -\lambda_x \lambda_y \\ -\lambda_x \lambda_y & \lambda_x^2 \end{bmatrix} \tag{28}$$

$$\tilde{P} = \frac{1}{\lambda_L \lambda_M} \begin{bmatrix} \lambda_L \lambda_M - \lambda_x^2 & -\lambda_x \lambda_y \\ -\lambda_x \lambda_y & \lambda_L \lambda_M - \lambda_y^2 \end{bmatrix} \tag{29}$$

Since both of these matrices are symmetric, the eigenvectors are orthogonal and repeated application of each projection can be summarized as

$$P^n u = \lambda_1^n \frac{u \cdot x_1}{x_1 \cdot x_1} x_1 + \lambda_2^n \frac{u \cdot x_2}{x_2 \cdot x_2} x_2 \tag{30}$$

where $x_1 = [\lambda_y, -\lambda_x]^{\mathrm{T}}$ and $x_2 = [\lambda_x, \lambda_y]^{\mathrm{T}}$ are the orthogonal eigenvectors corresponding to the eigenvalues λ_1 and λ_2, respectively. Since we are only concerned with the gradient of the Fourier component, the 'curl-free' modes $u = x_2$, we need only concern ourselves with this second eigenvalue and eigenvector. For the exact projection, $\lambda_1 = 1$ and $\lambda_2 = 0$ and there is no issue of a remnant divergence after the projection. However, for the approximate projection, λ_2 is non-zero.

The approximate projection has the eigenvalues $\lambda_1 = 1$ and $\lambda_2 = 1 - (\lambda_x^2 + \lambda_y^2)/(\lambda_L \lambda_M)$ with the same eigenvectors as the exact projection. Its approximate nature is reflected in the fact that λ_2 differs from zero. In Figure 1, λ_2 is plotted for Q1Q1 and P1P1, with and without mass lumping. Here we see that λ_2 is bounded between 0 and 1 for all four variants. Note that this eigenvalue is equal to one for several modes corresponding to $2\Delta x, 2\Delta y$, and $2\Delta x \Delta y$ modes. Fortunately, x_2 is zero for these modes and nearly zero for modes nearing these length scales as shown in Figure 2 for both P1P1 and Q1Q1. The tilt associated with P1P1 is an artifact of the orientation of the triangles which is shown in Figure 3. Hence for any well resolved modes the divergence is strongly controlled and modes that have a weak damping factor are barely supported by the gradient operator. Although not explored in this manuscript, this analysis is directly extendible to three dimensions, where the relevant eigenvalue and eigenvector are respectively, $\lambda_3 = 1 - (\lambda_x^2 + \lambda_y^2 + \lambda_z^2)/(\lambda_L \lambda_M)$ and $x_3 = [\lambda_x, \lambda_y, \lambda_z]$. In the next section, we illustrate these properties in a periodic case where these analytic results are directly applicable.

2.3. Comparison with other projections

Before presenting the numerical results, we explore the relationship of Q1Q1 to other approximate projections. Gresho *et al.* [8] analysed an explicit form of this method that uses both lumped mass and $\theta = 0$. There they observed a stable integration using only a single projection of the acceleration. Although Gresho *et al.* were successful in simulating steady-state flow over a wing, ABC with a similar method observed noise in the velocity field during long time integrations. Another method very similar to this one is given by Codina [9] and utilizes the same form of the mass matrix, but achieves stabilization by adding an additional factor to the pressure gradient term. Guermond presents a summary of several projection methods with error analysis techniques for evaluating them [10].

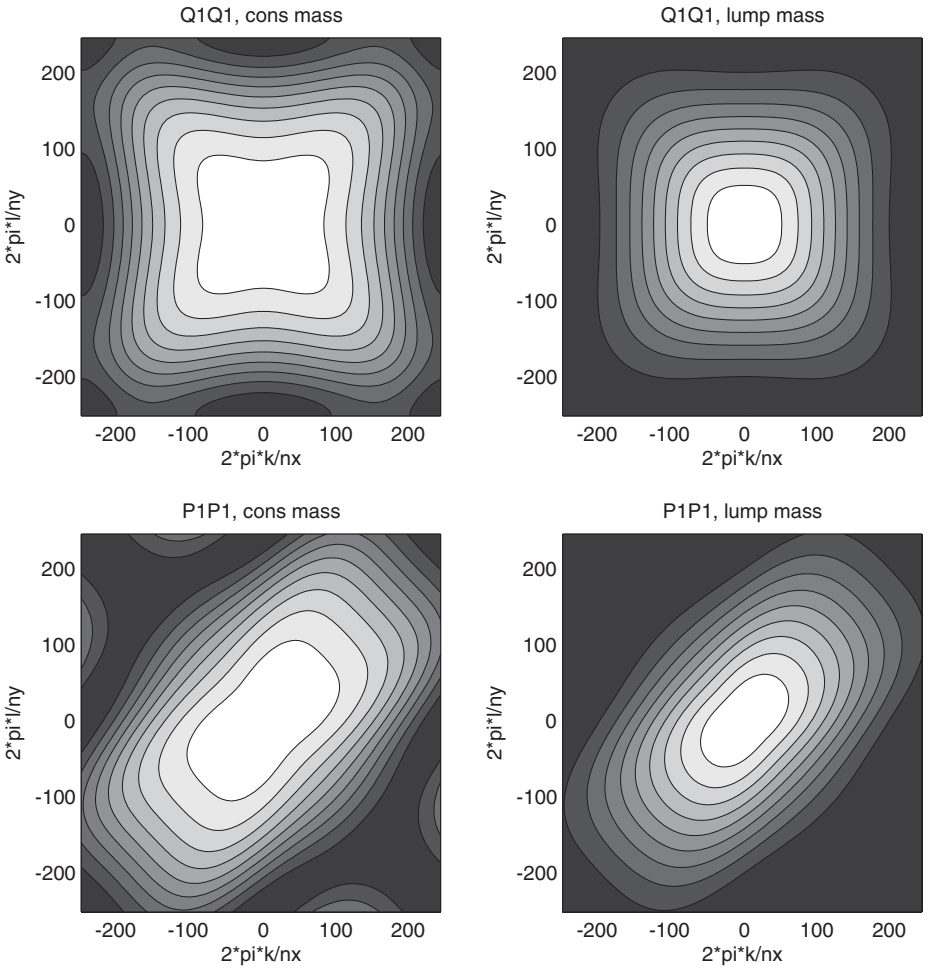

Figure 1. λ_2 for lumped mass, consistent mass, P1P1 and Q1Q1, contours start from 0.0 (white) and go to 1.0 (black) with 0.1 increments. 256 points were used in both x and y.

The approximate projection method most similar to our Q1Q1 is the well known PISO method of Issa [11]. In that method, one seeks to minimize the difference of the numerical solution from the desired relationships

$$\begin{aligned} u^{n+1} &= u^n + \Delta t M_l^{-1}(H^{n+1} - Gp^{n+1}) \\ DGp^{n+1} &= DH^{n+1} \end{aligned} \tag{31}$$

where $H^{n+1} = -(K + N(u^n))(u^{n+1})$. PISO is a finite difference approach that is designed to approximate a simultaneous equation solver of both velocity and pressure and although this is only first order in time, higher order temporal accuracy would complicate its use as a

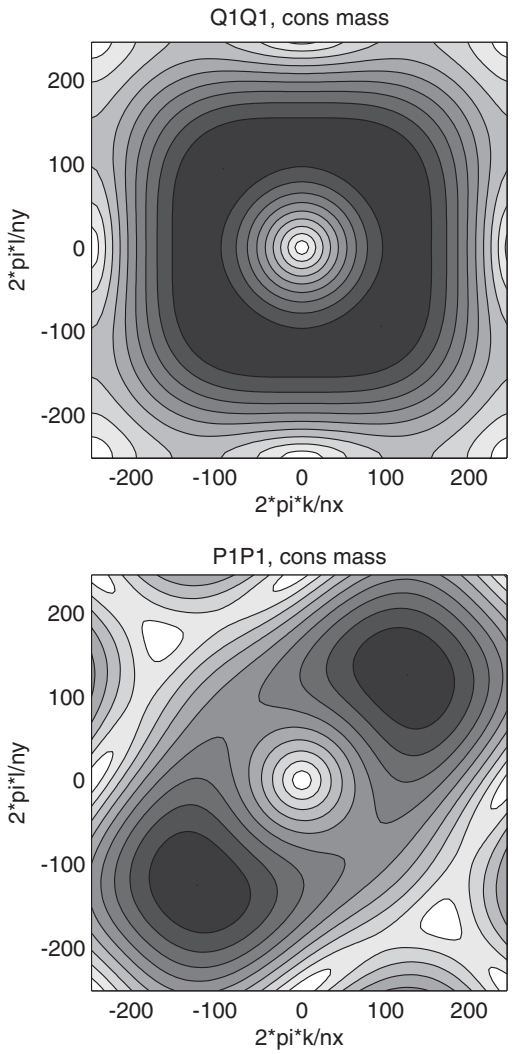

Figure 2. Norm of $x_2/\max(x_2)$ for P1P1 and Q1Q1. Contours start from 0.0 (white) and go to 1.0 (black) with 0.1 increments.

steady-state integration method. Our atmospheric applications are inherently time accurate and the higher-order temporal corrections are essential. Ignoring these differences, our method can be made to have a similar form as PISO while retaining second order in space and time accuracy by using the following two additional steps. Instead of using $H^{n+1/2}$ in the second projection, one can use the updated forcing as $H_{\text{new}}^{n+1/2} = -(K + N(u^{n+1/2}))((u^n + u^{n+1})/2)$. Then one can solve for the pressure to the same tolerance as in the first projection and apply the gradient of this pressure to obtain the final velocities. In the results section, we will compare our method with and without these extra steps to the base method to establish its relationship with PISO.

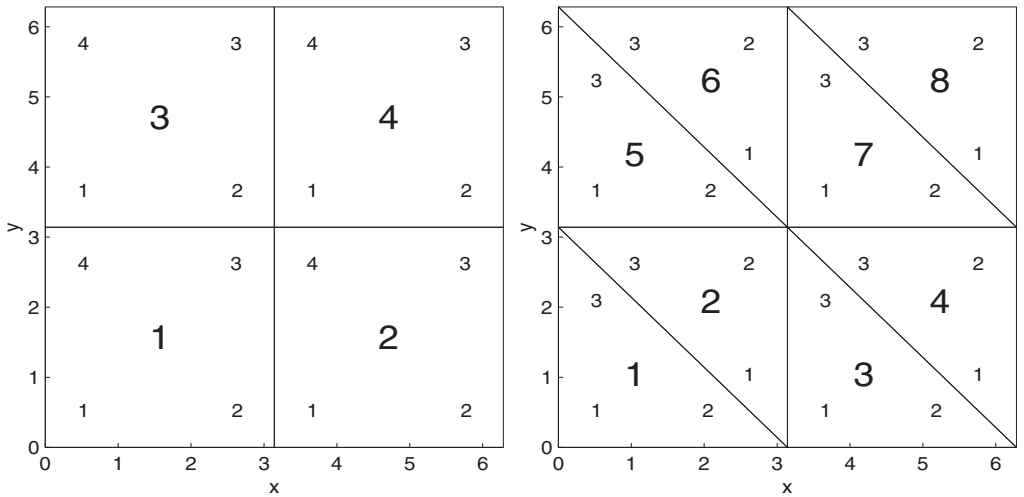

Figure 3. Orientation and nodal numbering of Q1Q1 (left) and P1P1 (right) for the two analytic tests.

Our method is very similar, and in part motivated by the **P5** approximate projection presented in ABC. However, there are important differences arising from its finite element discretization, a full mass matrix, and its co-located variables. The ABC implementation used a structured quadrilateral mesh with considerable computational complexity due to the use of several mesh staggerings. This algorithm extends their theory to unstructured triangular/quadrilateral in 2D and tetrahedral/hexahedral meshes in 3D. This method is very useful for simulations involving complex geometry and unstructured meshes in that it only requires piecewise linear finite elements with all the variables co-located at nodal positions.

3. RESULTS

This section provides numerical examples which highlight different aspects of this method's performance. We use a periodic test with an analytic solution for the purpose of testing the order of convergence and the analytic theory of the previous section. It is also important to illustrate the utility of this method in real world flows. For this purpose, we compare our method with laboratory results for flow over a cubical obstacle and dispersion from a continuous point source in the obstacle's wake.

3.1. Analytic tests with sines

This test case was performed using both Q1Q1 and P1P1 with elements and nodes defined on the domain shown in Figure 3. Note that the triangular elements of P1P1 have many different possible orientations and we have chosen to orient the triangles in a repeating pattern. Although it has a directional bias, this pattern results in a uniform mass and transport operators for each computational node that is amenable to analysis. For this P1P1 test case, each basis and test function have a hexagonal support. If one alternates the orientation, the basis functions have alternating diamond and square supports.

This test compares the numerical solutions from P1P1 and Q1Q1 to an exact solution to the incompressible Equations (1) and (2) with a constant viscosity on the periodic domain $(0, 2\pi) \times (0, 2\pi)$. The exact solution is given by

$$u_{\text{ex}}(x, y, t) = 1 - 2e^{-\lambda t} \cos(x - t) \sin(y - t) \tag{32}$$

$$v_{\text{ex}}(x, y, t) = 1 + 2e^{-\lambda t} \sin(x - t) \cos(y - t) \tag{33}$$

$$p_{\text{ex}}(x, y, t) = -e^{-2\lambda t}(\cos(2(x - t)) + \cos(2(y - t))) \tag{34}$$

where $\lambda = 2K$. We performed this comparison with different resolutions ranging from 16 to 256 elements in each direction. Since for this test we are only analysing the error between the numerical and the exact solutions after a fixed time t, we are not concerned with trying to differentiate the spatial from the temporal error. The timestep is decreased by half with each doubling in resolution in order to keep the relative proportion of these errors the same. This is equivalent to keeping the initial maximum Courant number fixed (a value of 1.0 was used). The viscosity, K was fixed to keep the Reynold's number ($R_e = 6\pi/K$) at a value of 1000. By plotting error norms for both u and p, and the divergence on log–log plots with respect to resolution, one can obtain estimates of the order of accuracy of each numerical variant. In the following plots, we compare Q1Q1 versus P1P1 with and without consistent mass and with and without the velocity predictor in the advective terms. A sequence of runs using the traditional Q1Q0 approach with no velocity predictor and lumped mass is provided as well. This sequence is useful in determining the relative accuracy of the approximate projections.

The results for the L1 error norm of u and p at $t = \pi$ are quite striking. For the cases without the velocity predictor, the results are first order and the different methods eventually converge to the same errors as resolution is increased as seen in Figures 4 and 5. Only in the case where the predictor is used do we see the expected increase in accuracy due to consistent mass seen in simpler tests with a known velocity field and an advected scalar. Surprisingly, P1P1 performs remarkably well against the Q1Q1 variant with the same combination of mass consistency and velocity predictor. The lumped mass cases actually show P1P1 performing better than Q1Q1. The Q1Q0 results for lumped mass and no predictor are equivalent to Q1Q1 in accuracy with no predictor and lumped mass. This indicates that little is lost by switching from an exact to an approximate projection. It is worthwhile to mention the relative cost of a method with and without the velocity predictor. The predictor requires its own subtimestep with its own Poisson solve, effectively doubling the computational cost of a timestep. For this test case, the 32 point simulation with the predictor is equivalent in accuracy to the 256 point simulation without it. This results in a factor of 256 times more work without the predictor for this level of accuracy, due to the factor of 8 increase in cost with a doubling in resolution. This is a conservative estimate, since numerical linear algebra often does not scale linearly with increases in problem size.

The divergence results in Figure 6 reflect the eigenstructure in the previous theory section. In this case, the largest effect on the size of the numerical divergence is the choice of consistent mass which causes the greatest decrease in the size of the numerical divergence, a reflection of the data presented in Figure 1. The next largest effect is the choice of velocity predictor, and the choice of Q1Q1 versus P1P1 seemed to be the smallest effect. Note that the decrease in divergence for all variants is better than second order. This reflects the case that the low

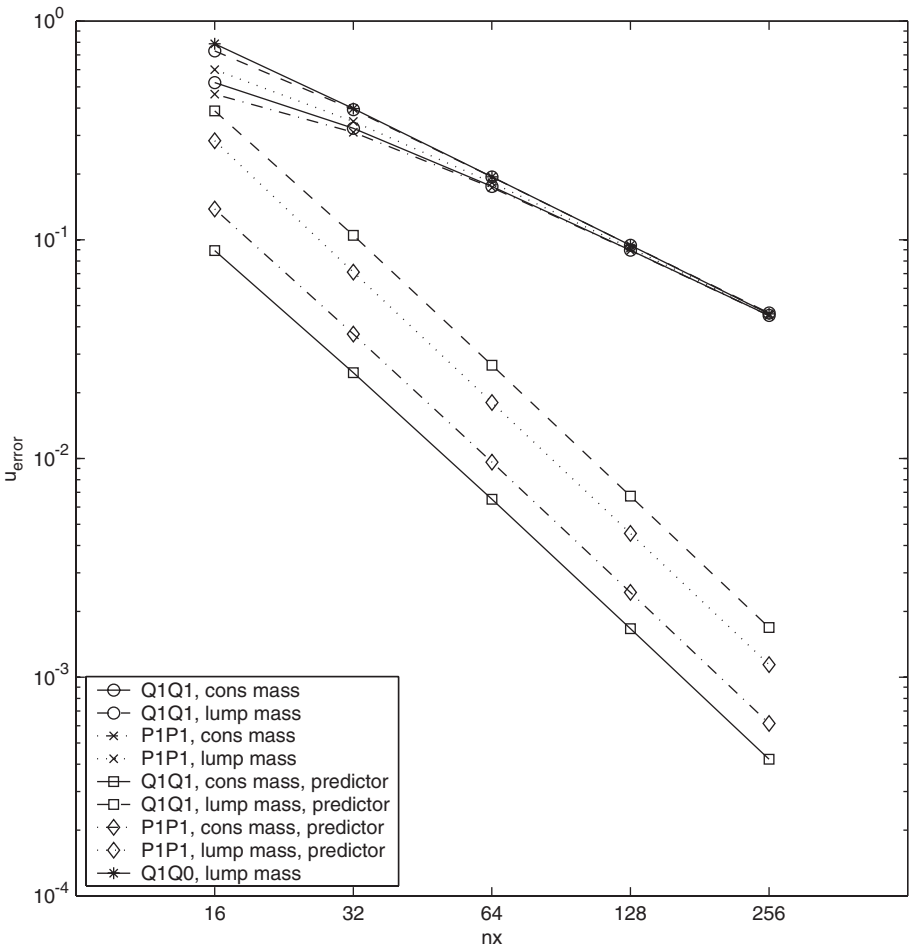

Figure 4. Velocity error for the translating vortex test, for several variations of Q1Q0, P1P1, and Q1Q1.

wavenumbers of the analytic solution are more and more resolved as the resolution is increased which decreases the value of λ_2 resulting in a faster than second-order convergence in the velocity divergence.

The comparison of this method with the PISO varient from the previous section is presented in Figures 7 and 8 for the error in the velocities and the numerical divergence, respectively. All combinations of (1) updating the velocity forcing and then (2) applying the gradient of the second gradient to the velocities were performed for the case of the method with predictor, consistent mass and Q1Q1. For the numerical divergence, it appears that, since step two is a projection of a forcing and the projection is approximate, applying this gradient to the velocities degrades the solution. It appears that step one had very little effect on this quantity. For the velocity error, it is a different story. There the findings are reversed and step two is more important in controlling the error. Step one appears to have a minor effect in

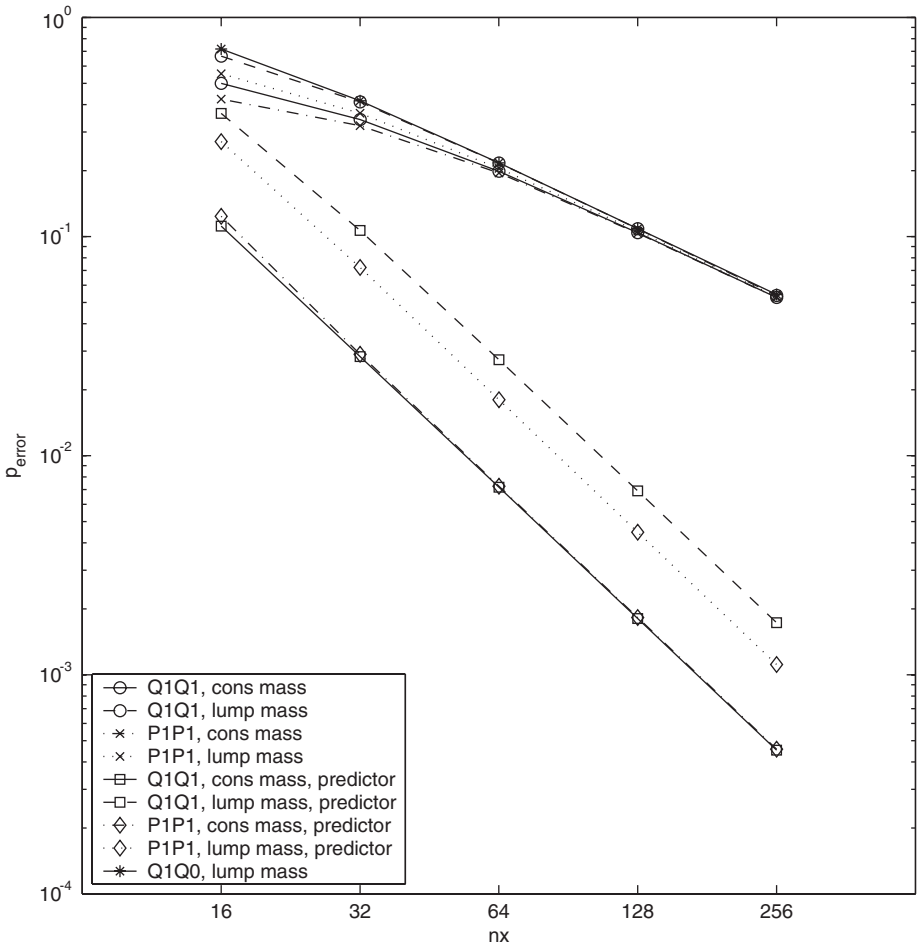

Figure 5. Pressure error for the translating vortex test, for several variations of Q1Q0, P1P1, and Q1Q1.

reducing the error when step two is also applied. Note that in this case the second projection was solved to 1.e − 8 as was the first projection for all the variants. As this increased the amount of work in the second projection by a factor of four, the use of step two could be problematic in situations where computational resources are limited. For this test case, step one alone resulted in approximately a 40% increase in accuracy at only the expense of another matrix–vector multiply.

3.2. Comparison with laboratory experiment

We are using Q1Q1 and Q1Q0 as the basis for a numerical model that predicts airflow and pollutant dispersal on building-scales from a single building to multi-building complexes; see Reference [12]. The prediction of atmospheric flow and pollutant dispersion in an urban area is difficult due to the presence of buildings and numerous other obstacles. Individual

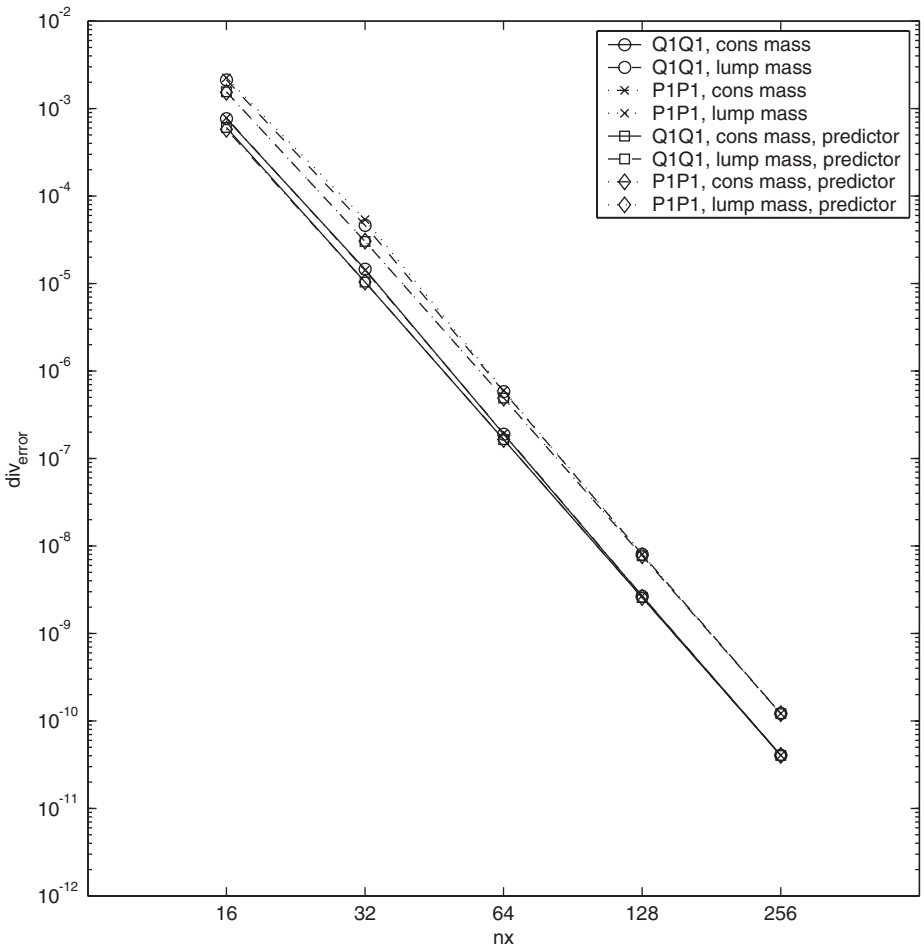

Figure 6. Numerical divergence for Q1Q1 and P1P1 for the translating vortex test. Q1Q0 not shown due to its numerical value of machine roundoff.

buildings exhibit significant geometrical variations with building wakes from adjacent buildings interfering with and altering the trajectory of street level plumes. The simple configuration of flow around a cubical obstacle is a fundamental test case for establishing the credibility of the model for use in the assessment of flow and dispersion of hazardous agents around buildings.

This paper uses two studies to evaluate the accuracy of our model for flow and dispersion. The fidelity of the model with respect to the flow field is judged by comparison with results from a laboratory experiment by Martinuzzi and Tropea [13]. There the non-dimensional velocity, U/U_0, where U is the stream-wise horizontal velocity field and U_0 is the mean inflow velocity, provides a useful metric for comparing the winds responsible for dispersion. The degree of variability in the flow can be judged via the normalized turbulent kinetic energy k/U_0^2. Turbulent kinetic energy (TKE) provides an estimate for the turbulent variations that occur in this flow as it is computed as a variance of actual velocities

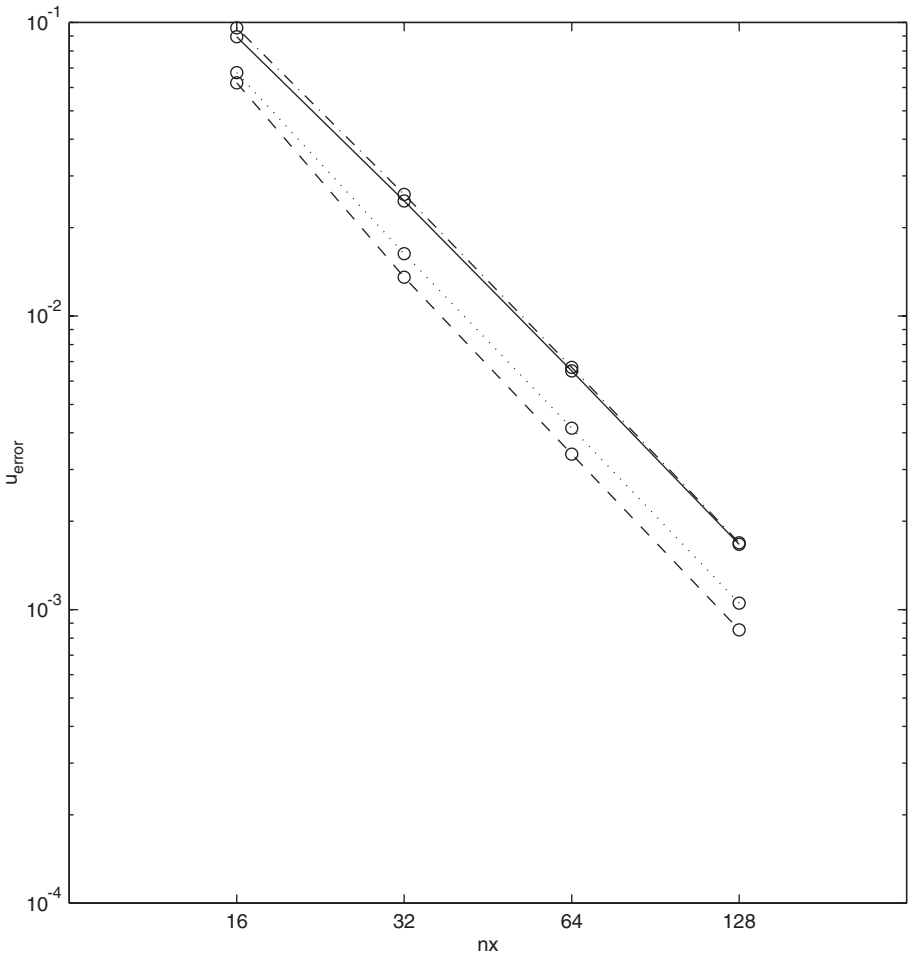

Figure 7. Velocity error for the translating vortex test for comparison with the PISO method. The dashed line represents updated velocities and forcings in a manner similar to PISO. The solid line updates only the forcing. The dotted line updates only the velocities. The dash-dot updates neither the forcing nor the velocities.

from their time-averaged mean value. With respect to dispersion, which for release assessment purposes is more important than the actual flow field itself, we use a study by Zhang *et al*. [14] who released a ground level tracer $0.25H$ downstream from the cube where H is the height of the cube. The experiment showed that the tracer is entrained into the recirculating eddy behind the cube and dispersed downstream. An important feature of the dispersion pattern is that it quickly becomes much wider than the cube width within a few block heights downstream.

The simplest non-trivial LES turbulence model and the one used here is the Smagorinsky subgrid model [15, 16]. This model uses a simple down-gradient mixing-length relationship

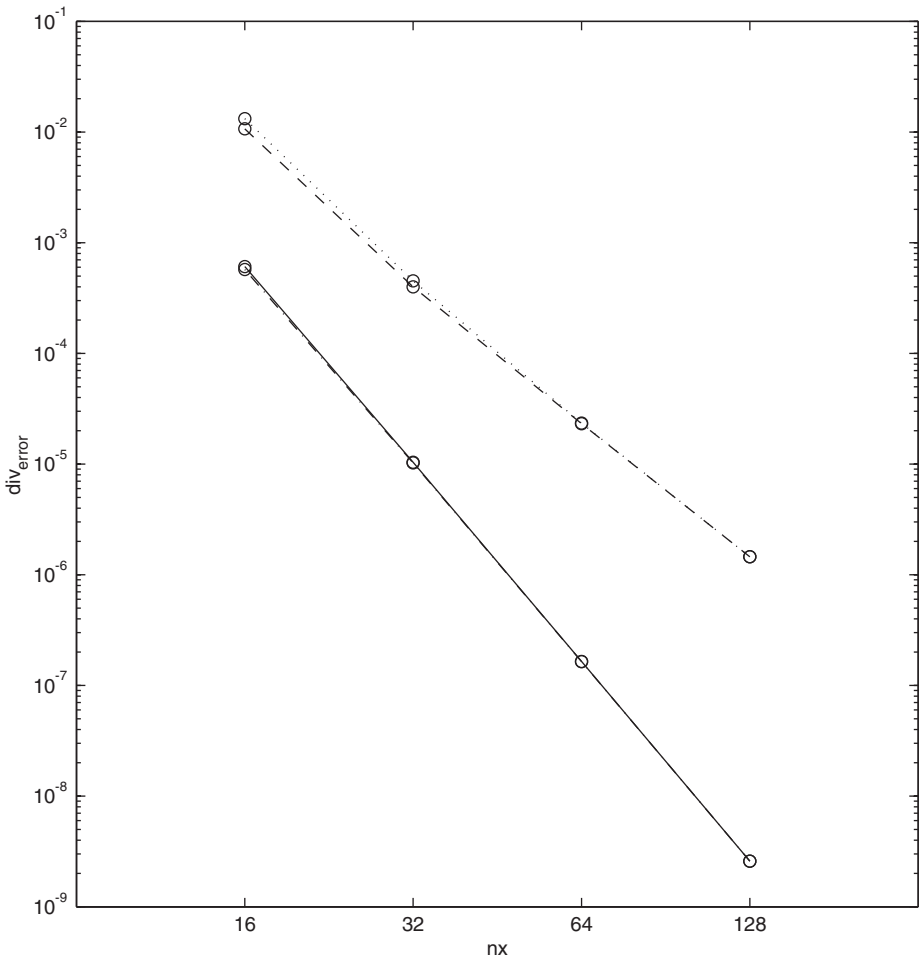

Figure 8. Numerical divergence for the translating vortex test for comparison with the PISO method. Line types are as in Figure 7.

between velocity and scalar gradients and the subgrid stress and fluxes

$$\overline{u_i' u_j'} = -K_m S_{ij} \tag{35}$$

$$\overline{u_j' c'} = -K_h \frac{\partial c}{\partial x_j} \tag{36}$$

The eddy viscosity is directly found from the equilibrium assumption that the subgrid turbulent kinetic energy is locally in equilibrium between locally generated shear production and dissipation and has the algebraic form:

$$K_m = \frac{c_s^2 l^2}{2} S_{ij} S_{ij} \tag{37}$$

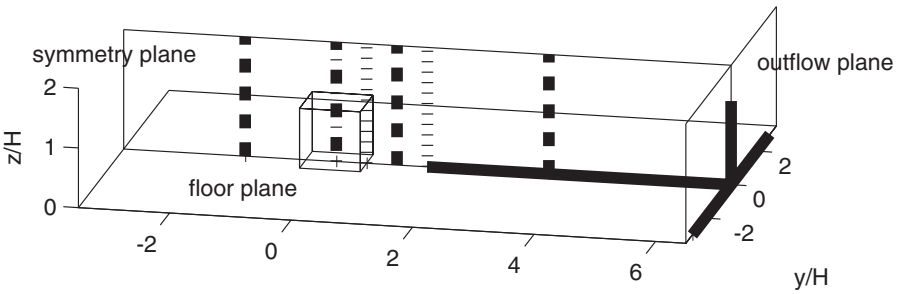

Figure 9. Flow domain and location of observational profiles. The thick dashed lines represent where velocity is compared, the thin dashed lines TKE, and the combination lines where both are. Dispersion of an advected scalar is compared at the thick solid lines against the experimental results of Zhang and Snyder.

where S_{ij} is the strain tensor. There are more complicated LES turbulence models such as the one by Deardorff [17], where this assumption is relaxed and subgrid turbulent kinetic energy is transported with the simulated flow. Piomelli [18] has also created a model which allows upscale transport of this quantity.

The computational domain was designed to be wide enough to contain the dispersion pattern observed by Zhang *et al.* [14] while keeping the resolution high enough to provide good comparison with the flow data of Martinuzzi and Tropea. The fundamental length scale in this investigation is the height of the cube H which we take to be 1 m. The computational domain is a rectangular channel of height $2H$, width $7H$ and length $10H$. The origin is situated at the center of the cube, with the inflow at $x=-3.5H$. Over the entire inflow, the inflow velocity was a constant 0.6 m/s. This agrees with the inflow profile of Zhang *et al.* where all of the turbulence was generated by a cube mounted to a flat plate which was towed in a water tunnel. The flow domain is illustrated in Figure 9. This figure displays the cube and several vertical and horizontal lines where profiles from both the experiments of Zhang and Snyder and Martinuzzi and Tropea are presented. The simulations are compared against the mean velocity and TKE profiles of Martinuzzi and Tropea. The thick dashed lines represent where velocity is compared, the thin dashed lines TKE, and the combination lines where both are. Dispersion of an advected scalar is compared at the thick solid lines against the experimental results of Zhang and Snyder.

Figures 10 and 11 compare the time mean streamwise velocity and turbulent kinetic energy at the symmetry plane with the experimental results of Martinuzzi and Tropea [13]. The main features of all flow fields are similar. They include the separation zones in front of the cube, on the roof and the two sides, a primary recirculation zone in the wake, and a pair of counter-rotating vortices on the horizontal plane (not shown). The recirculation length of the Q1Q0 simulation was 1.55 and that of Q1Q1 was 1.5. This agrees well with the value of 1.68 measured by Martinuzzi and Tropea. These lengths compare more favourably than that predicted by the simpler, but widely used standard k–ε turbulence model results that tend to be around 2.85 [19]. The features of both simulations agree well with the experimental data with respect to the velocities in Figure 10. The small discrepancies at the top of the domain are generated by the free slip boundary conditions used in the numerical

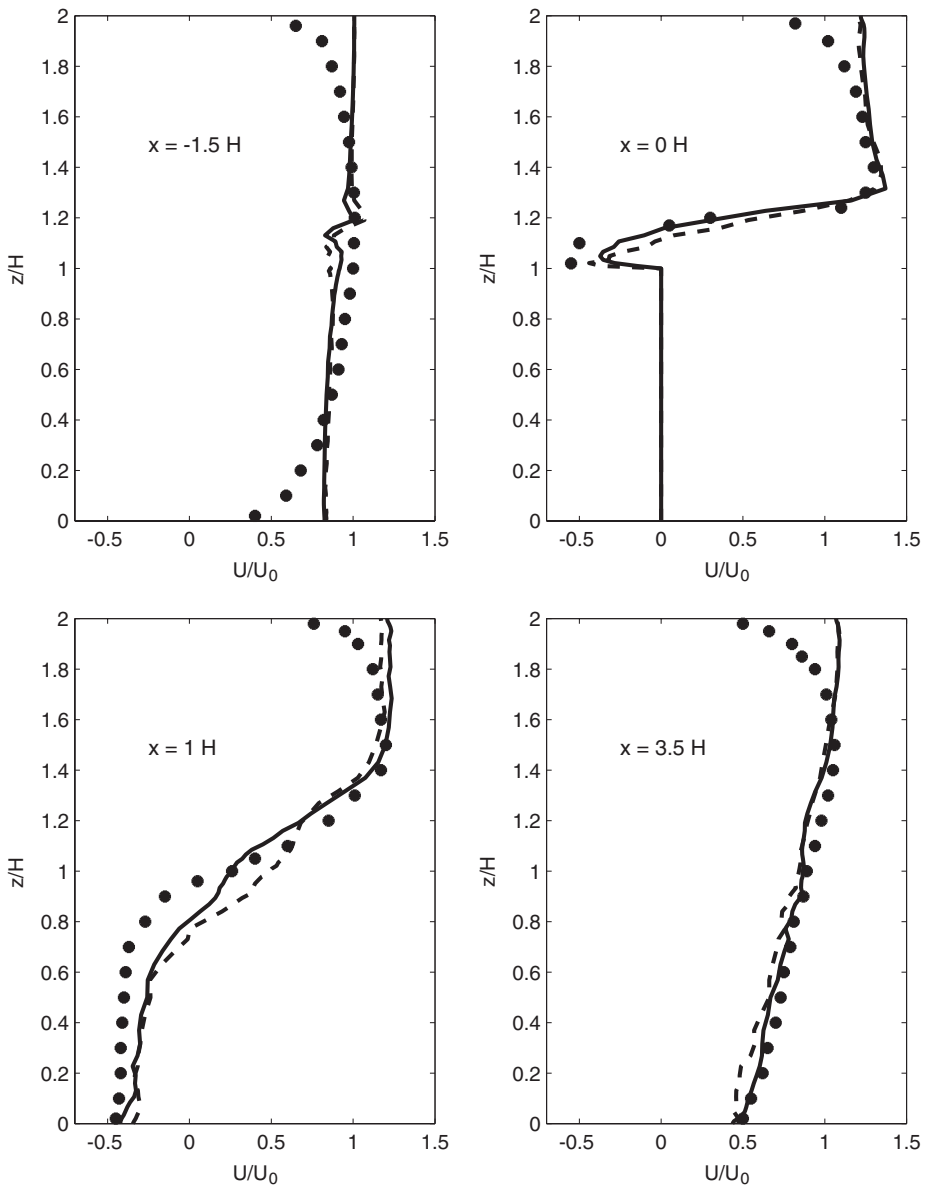

Figure 10. Mean streamwise velocity at four locations along the symmetry plane. The dots are from Martinuzzi, the solid line from Q1Q1 and the dashed from Q1Q0.

simulations to approximate the higher top boundary location of the Zhang *et al.* [14] dispersion experiment.

The results of Zhang *et al.* [14] are used to evaluate the accuracy of concentration patterns from the model. These results were created with a tow tank in which a cube mounted to a plate was moved at 0.6 m/s through a water tank 18 m long. The cube was 0.1 m high and

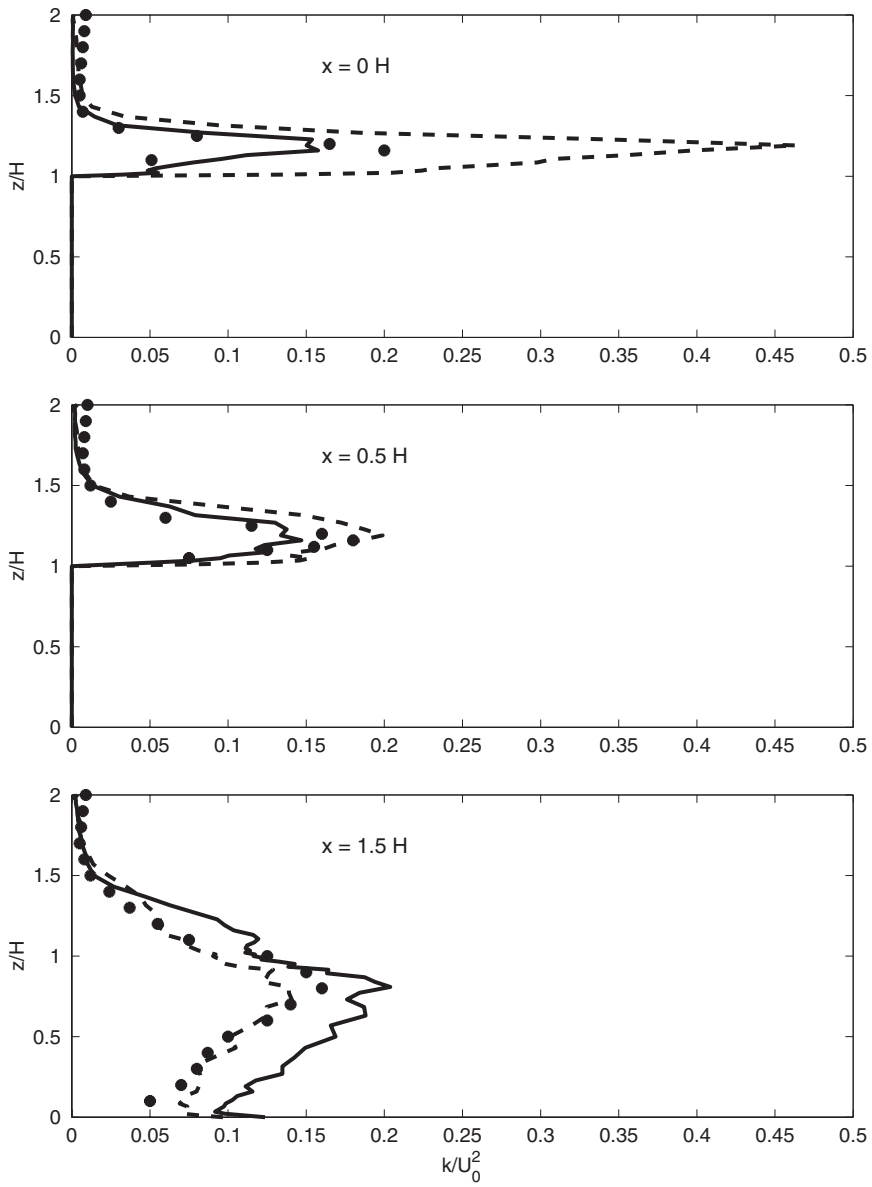

Figure 11. Total turbulent kinetic energy at three locations along the symmetry plane. The dots are from Martinuzzi, the solid line from Q1Q1 and the dashed from Q1Q0.

the tank was 1 m wide by 1 m. All of the turbulence in the experiment was generated by the passage of the cube. The dispersion in their experiments is generated by a small ground-level continuous source $0.25H$ centered behind the rear of the cube. The solid thick lines of Figure 9 are the locations where the concentrations downstream from the cube have been measured. Although both simulations used much smaller domains than this experiment, it appears that

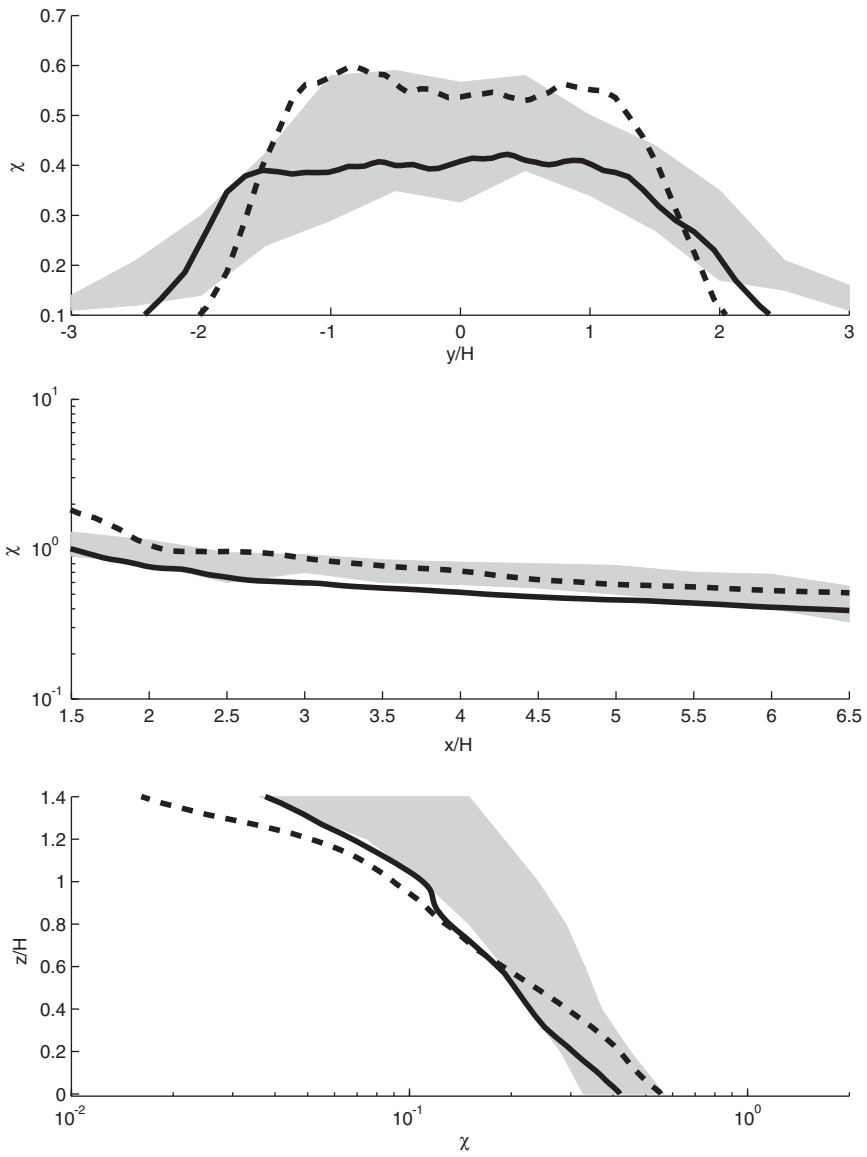

Figure 12. Comparison of tracer profiles with experiment. The experimental range is shown as a gray area, the Q1Q0 LES result as a dashed line and the solid line is the Q1Q1 result. The top plot is for the profile along the floor of the outflow, the middle plot is the profile along the floor of the symmetry plane, and the bottom plot shows a vertical profile in the symmetry plane at the outflow.

capturing the vortex shedding behind the cube is the most important factor in determining the concentration pattern in the wake of the building.

In Figure 12, we show the profile comparison along the thick solid lines of Figure 9. We see good agreement for both numerical methods. The top plot shows the simulations both

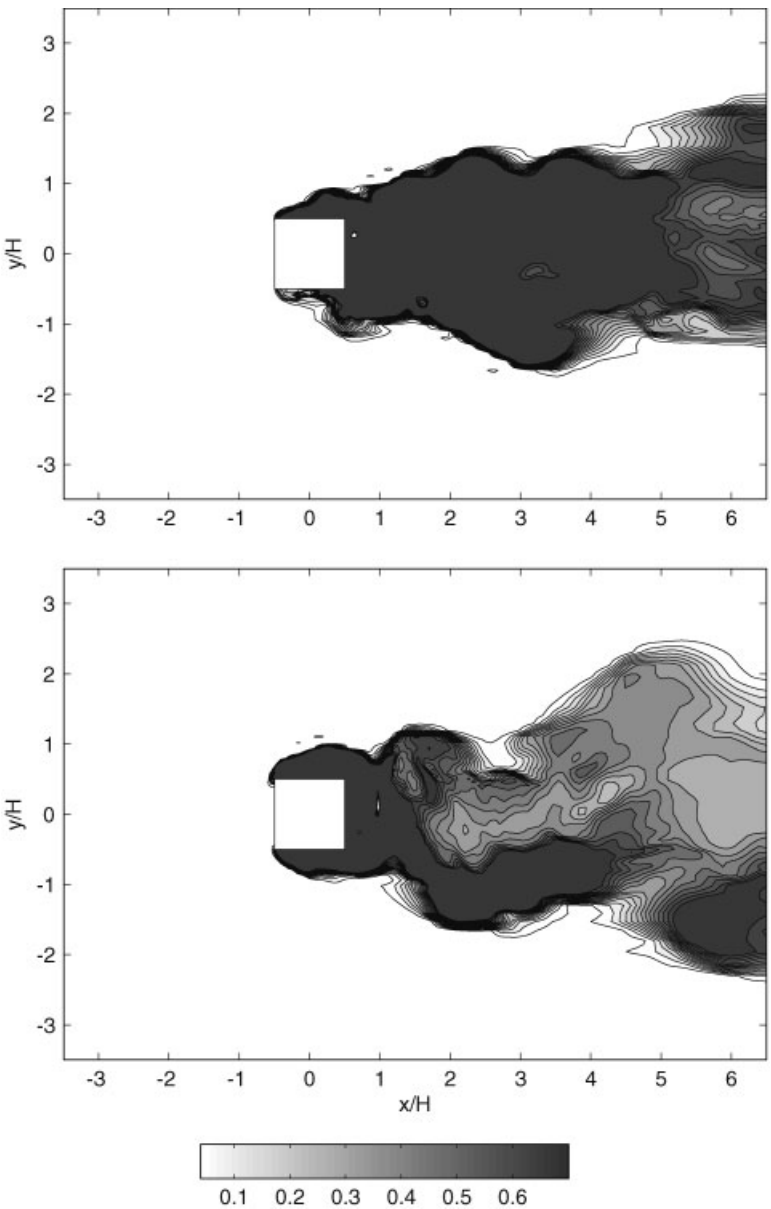

Figure 13. Instantaneous tracer snapshots on the ground surface. The top contour plot shows Q1Q0 and the bottom Q1Q1.

capturing the horizontal dispersion at the outflow found in the observations. The middle plot shows the simulations agreeing with experiment along the bottom of the symmetry plane. The bottom plot shows a vertical concentration profile centered in the middle of the outflow plane. Here it appears that Q1Q1 is more accurately capturing the observed dispersion. The Q1Q1

simulation is able to spread more of the tracer in the vertical and horizontal to get better agreement with experiment, whereas the Q1Q0 simulation predicted a plume that was more concentrated at the centerline directly behind the cube. A possible reason for this is seen in overhead snapshots looking down at the surface tracer concentrations as shown in Figure 13, where we compare Q1Q0 and Q1Q1 plumes. It appears that the Q1Q1 approach tends to have more active vortex shedding than the Q1Q0 approach which could account for its wider dispersion pattern.

4. CONCLUSION

We have presented comparisons of Q1Q1, P1P1 and Q1Q0 for two numerical examples. In these comparisons, we have shown the co-located method to be equivalent in accuracy to the staggered Q1Q0 approach without 'checkerboarding' or other artifacts commonly observed with such non-staggered methods. The major utility of this method has not yet been discussed, but becomes apparent when we discuss the engineering utility of this co-located method. Its construction involves less complexity than Q1Q0 as the Laplacian matrix L is the constant viscosity diffusion matrix K and hence the conversion of a Q1Q0 method to Q1Q1 is straightforward. For unstructured models, only one set of connectivity is required which often eliminates the need to store multiple matrices. For the case of P1P1 on triangles and tetrahedrons, one can completely eliminate the need to store the matrices as they can be integrated exactly. For the Q1Q1 simulation of the cube, only one matrix was required as the same storage was used in the solution process of Equations (11), (12) and (14). Finally, L is a standard finite element Laplacian (the 5 point Laplacian for P1P1) and is much more amenable to iterative solution techniques such as algebraic multigrid which can often be rendered virtually unusable by ill-conditioning in the case of $G^{\mathrm{T}}M_L^{-1}G$. We are currently performing parameter studies with multiple linear algebra techniques to determine how to optimally take advantage of the better conditioning of L with respect to $G^{\mathrm{T}}M_L^{-1}G$.

This method is of practical utility to mesh refinement techniques as well. Many structured adaptive mesh refinement techniques (often denoted by AMR) suffer from ad-hoc methods of transferring coarse data to fine levels of refinement. By collocating all of the variables, established techniques such as finite volume-element method (FVE) and fast adaptive composite (FAC) introduced by McCormick [7] can be applied to all of the variables in complex systems of equations. Coarse–fine interfaces can for example make use of the ability of this method to use both triangles and quadrilaterals for instance to rigorously constrain the discretization at these junctures. By putting them on a solid theoretical foundation, this could have dramatic improvements in the fidelity and performance of such models.

ACKNOWLEDGEMENTS

This work was performed under the auspices of the U.S. Department of Energy by the University of California, Lawrence Livermore National Laboratory under contract No. W-7405-Eng-48.

REFERENCES

1. Almgren AS, Bell JB, Crutchfield W. Approximate projection methods: part I. inviscid analysis. *SIAM Journal on Scientific Computing* 2000; **22**:1139–1159.

2. Gresho PM, Chan ST. Projection 2 goes turbulent and fully implicit. *International Journal of Computational Fluid Dynamics* 1998; **9**:249.
3. Sani RL, Gresho PM, Lee RL, Griffiths DF. The cause and cure (!) of the spurious pressures generated by certain FEM solutions of the incompressible Navier–Stokes Equations, Part 1. *International Journal of Computational Fluid Dynamics* 1981; **1**:17–44.
4. Sani RL, Gresho PM, Lee RL, Griffiths DF, Engelman M. The cause and cure (!) of the spurious pressures generated by certain FEM solutions of the incompressible Navier–Stokes Equations, Part 2. *International Journal of Computational Fluid Dynamics* 1981; **1**:171–204.
5. Silvester DJ, Kechkar N. Stabilized bilinear-constant velocity-pressure finite elements for the conjugate gradient solution of the Stokes problem. *Computational Methods in Applied Mechanics and Engineering* 1990; **79**: 71–86.
6. Gresho PM, Sani RL. *Incompressible Flow and the Finite Element Method*. Wiley: New York, 2000.
7. McCormick S. *Multilevel Adaptive Methods for Partial Differential Equations*. Frontiers in Applied Mathematics, vol. 6. SIAM: Philadelphia, PA, 1989.
8. Gresho PM, Chan ST, Christon MA, Hindmarsh AC. A little more on stabilized Q1Q1 for transient viscous incompressible flow. *International Journal for Numerical Methods in Fluids* 1995; **21**:837–856.
9. Codina R. Pressure stability in fractional step finite element methods for incompressible flows. *Journal of Computational Physics* 2001; **170**:112–140.
10. Guermond J-L, Tenaud C. Error Analysis and numerical tests for the approximation of unsteady incompressible viscous flows by means of projection methods. *Proceedings of the ECCOMAS 94*. Wiley: Chichester, England, 1994.
11. Issa RI. Solution of the implicitly discretized fluid flow equations by operator-splitting. *Journal of Computational Physics* 1985; **62**:40–65.
12. Chan ST, Stevens DE. Two advanced turbulence models for simulating the flow and dispersion around buildings. *Proceedings of the Millennium NATO/CCMS Int. Tech. Meeting on Air Pollution Modeling and its Application* Boulder, CO, 2000; 355–366.
13. Martinuzzi R, Tropea C. The flow around surface-mounted, prismatic obstacles placed in a fully developed channel flow. *Journal of Fluids Engineering* 1993; **115**:85.
14. Zhang Y, Arya S, Snyder W. A comparison of numerical and physical modeling of stable atmospheric flow and dispersion around a cubical building. *Atmospheric Environment* 1996; **30**:1327–1345.
15. Smagorinsky J. General circulation experiments with the primitive equations: 1. The basic experiment. *Monthly Weather Review* 1963; **121**:1847–1859.
16. Lilly DK. On the numerical simulation of buoyant convection. *Tellus* 1962; **14**:148–171.
17. Deardorff JW. The use of subgrid transport equations in a three-dimensional model of atmospheric turbulence. *Journal of Fluids Engineering* 1973; **95**:429–438.
18. Piomelli U. High Reynolds number calculations using the dynamic subgrid-scale stress model. *Physics of Fluids A* 1993; **5**:1484–1490.
19. Chan ST, Lee RL. A model for simulating airflow and pollutant dispersion around buildings. *Proceedings of Air Pollution 99*, San Francisco, 1999; 39–48.

